Probing Topological Thermal Flux in Equilibrium Using Electron Beams

Jie Ma[1], Hongxing Xu,[3,2,*] and Deng Pan[1,2,†]

[1]*State Key Laboratory of Precision Spectroscopy, East China Normal University, Shanghai 200062, China*
[2]*Institute of Quantum Materials and Physics, Henan Academy of Sciences, Zhengzhou 450046, China*
[3]*School of Physics and Technology, Wuhan University, Wuhan 430072, China*

Near nonreciprocal media at finite temperature, fluctuating near fields exhibit imbalanced thermal populations in opposite directions, generating equilibrium topological thermal fluxes that circulate the media. While the existence of these fluxes remains unconfirmed, we propose exploiting their interaction with free electron beams for detection. We establish a general framework to quantify thermal flux at any location near an object of arbitrary shape. This reveals unexplored properties of thermal flux spectra depending on their orientation. Further, we connect the electron scattering rate to the equilibrium thermal flux. As a specific example, electrons encountering a planar surface's perpendicular thermal flux preferentially scatter transversely. This measurable scattering distribution, i.e., via angle-resolved electron microscopy, allows us to recover the thermal flux spectrum. Additionally, electron interactions with equilibrium thermal fluxes surrounding local structures offer a novel approach to generating electron vortex beams.

Introduction—Optical near-field nonreciprocity arises when a magnetic field, applied perpendicular to the wave vector but parallel to the near field's spin [1,2], disrupts the dispersion symmetry for opposite propagation directions. This phenomenon is observed in magneto surface plasmons (SPs) [3–8], resulting in a one-way band gap, albeit not rigorously defined at the nonlocal limit [9]. True one-way band gaps necessitate the breaking of time-reversal symmetry in photonic crystals [10–14], akin to electron quantum Hall states, featuring unidirectional propagation and immunity to scattering.

Beyond coherent light, optical nonreciprocity surprisingly results in persistent thermal flux in equilibrium (TFE) within the optical near field [15–18]. This TFE arises from imbalanced thermal population of modes propagating in opposite directions. Specifically, the asymmetric dispersion of nonreciprocal near fields results in uneven photonic density of states, leading to a net thermal power flow when populated thermally. As this power flow transports energy, the TFE must follow closed trajectories around a finite body, rendering it topologically protected [16–18]. Otherwise, energy would accumulate and dissipate elsewhere, violating equilibrium.

Given such TFE, a natural question arises: can it exert a mechanical force on small objects or particles within its range? However, when the entire system under investigation is in thermal equilibrium, no significant effects can be anticipated [19]. In contrast, nonequilibrium scenarios offer opportunities for observations [19–22]. For instance, thermal torques or forces are predicted on magnetized particles at different temperatures from their environment [20,21], on two planar plates with different temperatures [22], or on a particle situated above a magneto-optical (MO) surface [19]. Additionally, TFE on an MO material has been shown to induce an electric current in adjacent graphene at a different temperature [23].

Instead of relying on nonequilibrium conditions to exploit TFE for mechanical effects, an alternative approach involves introducing small particles moving at relativistic speeds within the TFE. This configuration can lead to asymmetric dynamical Casimir friction [20,21] on neutral particles. Electrons, being easily accelerated to relativistic speeds compared to neutral nanoparticles, offer a more important means of analyzing near-field properties. The interaction of electrons with optical near fields excited by coherent light has opened up a new and exciting field [24–44]. Meanwhile, electron interactions with thermal fields, though less explored than their interaction with coherent light fields, can also give rise to intriguing phenomena [44–46].

In this Letter, we propose a feasible approach to probe the spectrum of the TFE using electron beams. This involves measuring the energy and transverse momentum distribution of the scattered electrons with currently attainable techniques [47,48]. When electron beams interact with the TFE, they are preferentially scattered transversely, inducing a transverse current that can be utilized to reconstruct the TFE spectrum. Moreover, the directional scattering of electrons interacting with the TFE surrounding
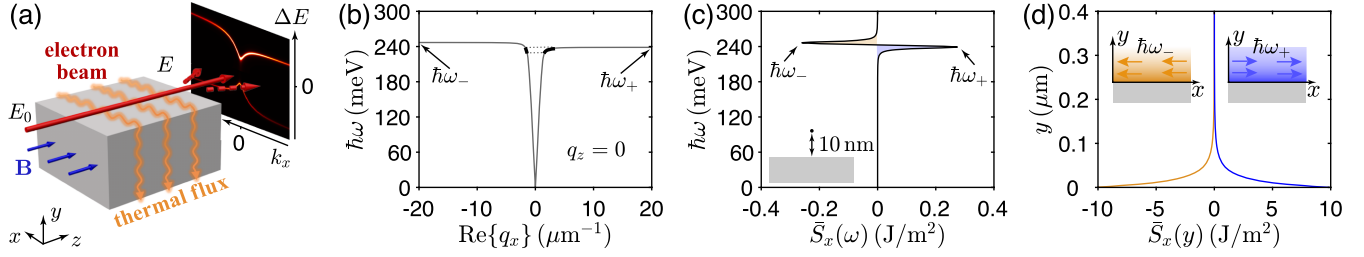
FIG. 1. (a) Electron beam scattering by TFE on a planar InAs surface under a static magnetic field $(+\hat{\mathbf{z}})$. The induced TFE (depicted by orange arrows) is perpendicular to the magnetic field. The incident electron beam (red arrow) travels along $+\hat{\mathbf{z}}$ with energy E_0. Deflected electrons with energy $E = E_0 - \Delta E$ exhibit an asymmetric distribution in final transverse momenta $\hbar k_x$ due to absorption or emission of thermal photons from the TFE. (b) Asymmetric dispersion relation of SP modes propagating along $\hat{\mathbf{x}}$ on the planar InAs surface shown in (a). (c) TFE spectrum at a point $(y = 10$ nm$)$ above the InAs surface. (d) Spatial distributions of TFE at the two resonance frequencies. The parameters for InAs are provided in the paragraph, and the magnetic field is $B = 2$ T. The temperature in (c) and (d) is $T = 300$ K.

local structures offers a new way to generate electron vortex beams.

Electron deflection by TFE—To illustrate the emergence of topological TFE around nonreciprocal media and its detection using electron beams, we consider the scenario of an electron beam traversing near the planar surface of an MO medium [Fig. 1(a)]. In our subsequent detailed calculations, we select InAs as an illustrative example, with both the magnetic field and incident electron beams aligned along the $+\hat{\mathbf{z}}$ direction. The relevant elements of the permittivity tensor of InAs are given by $\epsilon_{xx} = \epsilon_{yy} = \epsilon_\infty - \omega_p^2(\omega + i\gamma)/\omega[(\omega + i\gamma)^2 - \omega_c^2]$, $\epsilon_{zz} = \epsilon_\infty - \omega_p^2/\omega(\omega+i\gamma)$, and $\epsilon_{xy} = -\epsilon_{yx} = (\epsilon_{xx} - \epsilon_\infty)i\omega_c/(\omega + i\gamma)$, which are determined by the plasma frequency $\omega_p = \sqrt{4\pi n_e e^2/m_e^*}$, the cyclotron frequency $\omega_c = eB/m_e^*c$, and the damping frequency $\gamma = e/m_e^*\mu$. We adopt parameters for InAs [49] with an effective mass $m_e^* = 0.028m_e$, carrier density $n_e = 1.6 \times 10^{-19}$ cm^{-3}, electron mobility $\mu = 8 \times 10^3$ cm^2 V^{-1} s^{-1}, and $\epsilon_\infty = 12.37$.

In the absence of magnetization, a planar surface supports a symmetric pair of SP modes, propagating in opposite directions. Magnetization disrupts this reciprocity, introducing asymmetry in their dispersion. For instance, SP modes with the same energy but propagating along $\pm\hat{\mathbf{x}}$ directions exhibit distinct wave vectors, as shown in Fig. 1(b). Specifically, their resonant frequencies differ, opening a topologically protected one-way band gap (although not rigorous) $(\omega_+ < \omega < \omega_-)$. This nonreciprocity is most pronounced for modes propagating perpendicular to the magnetic field [$\hat{\mathbf{x}}$ direction, Fig. 1(b)], while it vanishes for the $\hat{\mathbf{z}}$ direction.

At finite temperature T, all SP states are populated according to the Bose-Einstein distribution function $n(\omega) = (e^{\hbar\omega/k_B T} - 1)^{-1}$. In the reciprocal scenario, contributions from counterpropagating modes cancel out, resulting in vanishing TFE. However, when magnetization breaks the reciprocity, modes propagating along the opposite directions around the same frequency are equally

populated, but they possess unequal densities of states and contributions to the power flow due to their distinct wave vectors [see short black lines, Fig. 1(b)]. These asymmetries combine to generate a nonzero net TFE. For the planar interface where SPs adhere to the symmetry $\omega(q_x, q_z) = \omega(q_x, -q_z)$, the resulting TFE is perpendicular to the magnetic field [orange arrows, Fig. 1(a)].

We propose utilizing electron beams to probe this TFE. As depicted in Fig. 1(a), a swift electron beam traversing near above the MO interface interacts with the TFE, causing asymmetric scatterings of the electrons and a transverse net current along the $\hat{\mathbf{x}}$ direction. This can be intuitively understood as the deflection of the electrons by the TFE. Detailed analysis of scattering probabilities across final state energies E enables recovery of the TFE spectrum [right panel, Fig. 1(a)].

General theory for TFE—The calculation of TFE has been approached by mode coupling theory in specific structures [15] or from the perspective of field quantization [16–18]. We here present a comprehensive formula for calculating the spectrum of TFE at any point surrounding an object of arbitrary geometry [50]. In systems at equilibrium, the fluctuating thermal fields are governed by the fluctuation-dissipation theorem (FDT). In a general scenario involving nonreciprocity, the electric field-electric field correlation is given by $\langle \hat{\vec{\mathcal{E}}}(\mathbf{r}, \omega) \otimes \hat{\vec{\mathcal{E}}}^\dagger(\mathbf{r}', \omega') \rangle = 2\pi\delta(\omega - \omega')\langle\hat{\vec{\mathcal{E}}}(\mathbf{r}) \otimes \hat{\vec{\mathcal{E}}}^\dagger(\mathbf{r}')\rangle_\omega$, where

$$\langle \hat{\vec{\mathcal{E}}}(\mathbf{r}) \otimes \hat{\vec{\mathcal{E}}}^\dagger(\mathbf{r}') \rangle_\omega = 2\hbar[n(\omega) + 1]\mathbb{G}(\mathbf{r}, \mathbf{r}', \omega), \quad (1)$$

where $\hat{\vec{\mathcal{E}}}$ is the electric field operator [50–53], $\langle \cdots \rangle$ denotes the ensemble average, and $\mathbb{G}(\mathbf{r}, \mathbf{r}', \omega) = [G(\mathbf{r}, \mathbf{r}', \omega) - G^\dagger(\mathbf{r}', \mathbf{r}, \omega)]/2i$ is the non-Hermitian part of the conventional electromagnetic Green tensor $G(\mathbf{r}, \mathbf{r}', \omega)$.

The power flux is characterized by the operator $\hat{\mathbf{S}} = c(\hat{\vec{\mathcal{E}}} \times \hat{\mathbf{H}}^\dagger + \hat{\vec{\mathcal{E}}}^\dagger \times \hat{\mathbf{H}} + \text{H.c.})/8\pi$, where $\hat{\mathbf{H}}$ is the magnetic field operator. By expressing $\hat{\mathbf{H}}$ in terms of $\hat{\vec{\mathcal{E}}}$ and

evaluating $\hat{\mathbf{S}}$ using the FDT as described in Eq. (1), we obtain the expression for TFE [50],

$$\bar{S}_i(\mathbf{r}, \omega) = \frac{\hbar c^2}{\pi \omega} \sum_{j \neq i} \partial'_j \text{Im}\{\mathbb{G}_{ji}(\mathbf{r}, \mathbf{r}', \omega)|_{\mathbf{r}'=\mathbf{r}}\} n(\omega), \quad (2)$$

where $\bar{S}_i(\mathbf{r}, \omega) = \langle \hat{S}_i(\mathbf{r}) \rangle_\omega$, ∂'_j acts on the jth component of $\mathbf{r}'$, and we have eliminated the contribution of zero-point fluctuations [50]. In reciprocal case, the Green tensor satisfies the symmetric condition $G(\mathbf{r}, \mathbf{r}', \omega) = G^{\text{T}}(\mathbf{r}', \mathbf{r}, \omega)$, leading to zero flux at equilibrium.

TFE near an interface—We then apply Eq. (2) to calculate the TFE near an MO interface as illustrated in Fig. 1(a). The Green tensor for an interface can be expressed using the Weyl identity expansion [54], incorporating the reflection coefficients of the interface, i.e., $r_{\eta\nu}$ ($\eta, \nu = s, p$). Inserting this expansion into Eq. (2), the TFE above the interface reduces to [50]

$$\bar{S}_x(y, \omega) \approx \frac{c\hbar n(\omega)}{2\pi^2 q} \int_{q_\parallel > q} q_x \tilde{q}_y d^2\mathbf{q}_\parallel \text{Im}\{r_{pp}\} e^{-2\tilde{q}_y y}, \quad (3)$$

where $\mathbf{q}_\parallel = q_x \hat{\mathbf{x}} + q_z \hat{\mathbf{z}}$, $\tilde{q}_y = \sqrt{q_\parallel^2 - q^2}$, and $q = \omega/c$. In Eq. (3), we retain only the term involving the Fresnel coefficient r_{pp}, as the SP field is mainly longitudinal, making other terms negligibly small [50]. We solve the reflection coefficients in Eq. (3) using field continuities at the interface, similar to deriving Fresnel coefficients [50].

The near-field TFE on the MO interface calculated using Eq. (3) is shown in Figs. 1(c) and 1(d). At a given point, $\bar{S}_x$ exhibits two maxima with opposite directions near the SP resonance frequencies [Fig. 1(c)]. For frequencies up to ω_+, $\bar{S}_x$ points along $+\hat{\mathbf{x}}$ and increases as asymmetry rises near resonance. Within the one-way band gap ($\omega_+ < \omega < \omega_-$), the flux reverses to $-\hat{\mathbf{x}}$, as SP modes in this frequency range propagate only in this direction. This TFE decays exponentially along $\hat{\mathbf{y}}$ due to the evanescent nature of the contributing fields [Fig. 1(d)].

Electron beam interactions with TFE—In a gauge where the scalar potential vanishes, the electron-photon interaction Hamiltonian is given by $\hat{\mathcal{H}}_{\text{I}} = i\hat{\mathcal{E}} \cdot \hat{\mathbf{j}}/\omega$, where $\hat{\mathbf{j}}(\mathbf{r}_0) = -e\bar{\bar{m}}_e^{-1}[\delta(\mathbf{r} - \mathbf{r}_0)\hat{\mathbf{p}} + \hat{\mathbf{p}}^\dagger \delta(\mathbf{r} - \mathbf{r}_0)]/2$ is the current operator, $\hat{\mathbf{p}}$ is the momentum operator, $\bar{\bar{m}}_e = \{m_e, m_e, \gamma m_e\}$, $\gamma = 1/\sqrt{1 - v^2/c^2}$ is the Lorentz factor. Employing Fermi's golden rule and ensemble averaging using the FDT described in Eq. (1), the transition rate between two electron states, $|i\rangle$ and $|f\rangle$, is given by [50]

$$\frac{d\Gamma_{fi}}{dt} = \frac{d\Gamma_{fi}^0}{dt}[n(\varepsilon_{if}) + 1] \quad \frac{d\Gamma_{if}}{dt} = \frac{d\Gamma_{fi}^0}{dt}n(\varepsilon_{if}), \quad (4)$$

where

$$\frac{d\Gamma_{fi}^0}{dt} = \frac{2}{\hbar \varepsilon_{if}^2} \int d^3\mathbf{r} d^3\mathbf{r}' \mathbf{j}_{fi}^*(\mathbf{r}) \cdot \mathbb{G}(\mathbf{r}, \mathbf{r}', \varepsilon_{if}) \cdot \mathbf{j}_{fi}(\mathbf{r}'), \quad (5)$$

$\mathbf{j}_{fi} = \langle f|\hat{\mathbf{j}}|i\rangle$, $\varepsilon_{if} = \varepsilon_i - \varepsilon_f$, $\hbar\varepsilon_i$ and $\hbar\varepsilon_f$ are the eigenenergies of the electron states, with the assumption $\varepsilon_i > \varepsilon_f$. In fact, summing Γ_{fi}^0 over all possible final state yields the electron energy loss probability at $T = 0$. Additionally, averaging the photon absorption and emission described in Eq. (4) at the same energy account in the vacuum field contribution, characterized by a factor of $1/2$.

Electron scattering near interfaces—We utilize Eqs. (4) and (5) to analyze the scenario illustrated in Fig. 1(a). Assuming paraxial electron beams confined within a 2D thin film around the $\hat{\mathbf{y}}$ coordinate, the transition current is also confined within this film. We consider an initial state $\psi_i = \psi_y(y - y_0)e^{ik_0 z}$ scattered to a final state $\psi_f = \psi_y(y - y_0)e^{i(k_x x + k_z z)}$, where $|\psi_y(y - y_0)|^2 = \delta(y - y_0)$. Inserting these inputs into Eq. (5), we find the corresponding zero-temperature transition probability [50]

$$\Gamma^0(\omega, k_x) \approx \frac{e^2 L}{\pi \hbar v^2} \frac{\tilde{q}_y}{q_\parallel^2} \text{Im}\{r_{pp}\} e^{-2\tilde{q}_y y_0}, \quad (6)$$

where L is the interaction length. Similar to Eq. (3), only the r_{pp} term is retained here as the other terms are small [50]. Energy conservation ($\Delta E = \hbar\omega$) and momentum conservation ($\mathbf{q}_\parallel = \mathbf{k}_0 - \mathbf{k}$) are implicit. The transition probability at finite temperature can be determined similarly to Eq. (4).

The electron transition probabilities for various final energies and transverse momenta are shown in Fig. 2(a). Two distinct stripes in the Γ map correspond to the efficient emission (upper) or absorption (lower) of SPs. The emergence of these stripes can be understood using the nonrecoil approximation, where $\Delta E \approx \hbar\mathbf{v} \cdot (\mathbf{k}_0 - \mathbf{k})$ [55]. Here, the transferred energy $\hbar\omega$ and momentum $\hbar\mathbf{q}_\parallel$ form a simple relation $\omega = \mathbf{q}_\parallel \cdot \mathbf{v}$. The intersection of this line with the SP dispersion relation $\omega(\mathbf{q}_\parallel)$ [$\mathbf{q}_\parallel \| \hat{\mathbf{x}}$ is shown in Fig. 1(b)] results in the efficient SP emission or absorption along the specific direction denoted by k_x in Fig. 2(a). The minimum value of the involved SP energy, approximately 200 meV along $\hat{\mathbf{z}}$ ($k_x = 0$), can be further decreased by using a higher v. Notably, the asymmetric distribution of Γ reveals preferentially scattering toward either $+\hat{\mathbf{x}}$ or $-\hat{\mathbf{x}}$, generating a transverse electric current, as shown in Fig. 2(b). This current is determined as $J_x(\Delta E) = -J_0\gamma k_0^{-1} \int k_x dk_x \Gamma(k_x, \Delta E)$, where $J_0 = ev$. Remarkably, $J_x(\Delta E)$ closely mirrors $\bar{S}_x$ shown in Fig. 1(c), offering a way to experimentally reconstruct the TFE spectrum.

To understand this connection further, we examine two resonance energies, $\Delta E_\pm = \hbar\omega_\pm$, at the two emission peaks of $J_x(\Delta E)$ [dashed and dotted lines, Figs. 2(a)–2(c)]. At these energies, the transition probabilities [Fig. 2(c)]
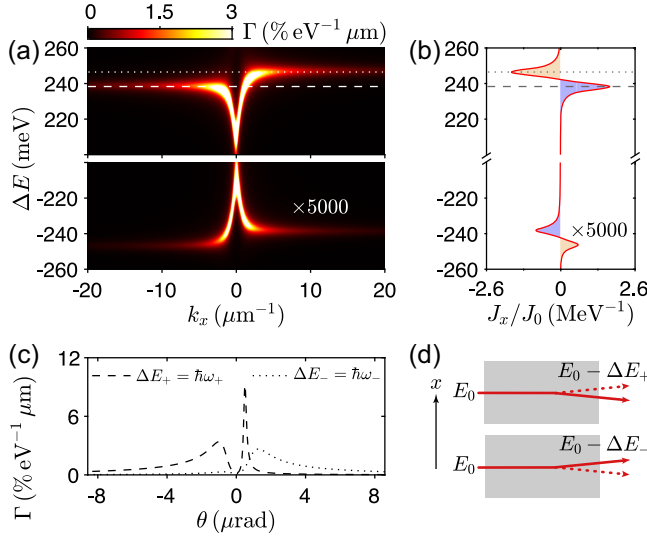
FIG. 2. (a) Electron scattering probabilities to final states with different energies ($E_0 - \Delta E$) and lateral momenta ($\hbar k_x$). (b) Current of scattered electrons in the $\hat{\mathbf{x}}$ direction, resulting from their asymmetric distribution over k_x shown in (a). (c) Sectional view of (a) for two resonance energies, $\Delta E_\pm$ [lines in (a) and (b)], with k_x converted to the deflection angle $\theta = \hbar k_x / m_e v$. (d) Illustration of asymmetric electron scattering. For output electron energies $E_0 - \Delta E_+$ and $E_0 - \Delta E_-$, electrons are preferentially scattered to $-\hat{\mathbf{x}}$ and $+\hat{\mathbf{x}}$, respectively, leading to opposite J_x in (b). The incident electron velocity is $v = 0.9c$, and the electron is located 10 nm above the interface. The interaction length is assumed to be $L = 1\,\mu\text{m}$. Other parameters are the same as in Fig. 1.

reveal that electrons preferentially release energy into SPs toward directions with higher mode densities. Momentum conservation dictates a backaction on the electrons, causing them to be preferentially deflected against the TFE direction [Fig. 2(d)]. Notably, within the "one-way" frequency range, the presence of only a $-\hat{\mathbf{x}}$ propagating branch deflects electrons entirely toward $+\hat{\mathbf{x}}$. Additionally, the precise transition rate incorporates the population function $n(\omega)$ [Eq. (4)]. Similarly, for the absorption peaks, the electrons tend to be deflected along the TFE direction. This interplay of asymmetric mode densities and thermal population, mirroring the mechanism underlying TFE, explains the remarkable consistency between $J_x(\hbar\omega)$ and $\bar{S}_x(\omega)$, validating our proposal of probing TFE using electron beams.

Interaction with TFE in local structure—While TFE on interfaces are expected to circulate around the boundaries [see Fig. 1(a)], reducing the structure size to the scale of the fluctuating fields can induce resonant effects, potentially unlocking new properties. Here, we explore this concept through the example of a hole punched on a freestanding InAs thin disk. We also demonstrate that interaction of electron beams with the TFE within this InAs nanohole can generate beams with orbital angular momentum (OAM) [56–60].

As illustrated in Fig. 3(a), we consider a thin InAs disk with a hole at its center, lying flat ($z = 0$) and serving as a
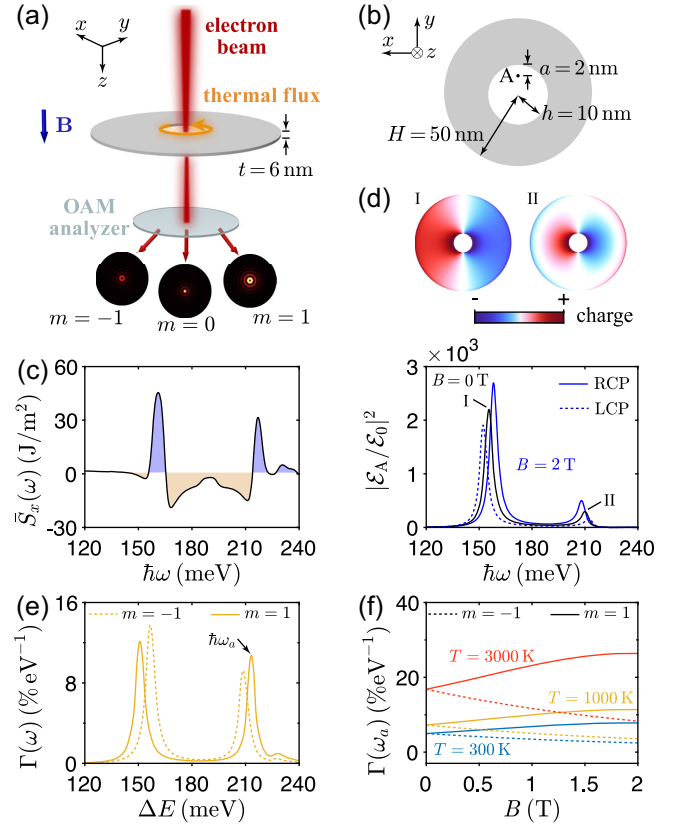

FIG. 3. (a) Illustration of a Gaussian electron beam interacting with the TFE (orange arrow) within a hole punched in a thin InAs disk, biased by a static magnetic field. An analyzer is placed after the disk to analyze the OAM carried by the scattered electrons. (b) Cross section of the disk. (c) The TFE calculated at point A [located at $(0, h - a, 0)$, see (b)]. (d) Lower: electric field enhancement at point A for illuminations of RCP/LCP light incident ($\mathcal{E}_0$) along the $+\hat{\mathbf{z}}$ direction. Upper: charge distributions at the two resonances. (e) Transition probabilities of electrons to states with different OAM $m\hbar$. (f) Dependence of the transition probabilities on the magnetic field and temperature for $\Delta E = \hbar\omega_a = 213$ meV. The waist of the incident beam is assumed to be $w = 3$ nm. Unless otherwise specified, other parameters remain consistent with those in Fig. 2.

structured two dimensional electron gas [50]. We model this disk classically, noting that while the nonlocal effect [61,62] can introduce minor corrections, it does not affect the essential physics [50]. A magnetic field applied along the $\hat{\mathbf{z}}$ axis induces a TFE circulating around the hole confined to the azimuthal direction due to rotational symmetry. Using Eq. (2) applied at a point on the $\hat{\mathbf{y}}$ axis [point A, Fig. 3(b)], with the Green function computed via the finite element method (FEM), we calculate the azimuthal component of TFE ($\bar{S}_x$ on this radius), as shown in Fig. 3(c). This TFE arises from the directional thermal flow of quasi-1D edge plasmons on the hole's edge, analogous to the directional thermal flow of SPs on the 2D surface in Fig. 1. Figure 3(d) (lower panel) displays the

electric field enhancement at point A when the disk is illuminated by right or left circularly polarized (RCP or LCP) plane waves (incident along $+\hat{z}$). Two resonance peaks are observed in the studied frequency range, formed by the bonding (I) and antibonding (II) coupling of edge plasmons on the outer circumference and around the hole [upper panel, Fig. 3(d)]. Both resonances are split for opposite circular polarizations by the magnetic field. Each pair of magnetically split edge plasmon resonances induce a range of clockwise or anticlockwise TFE [Fig. 3(c)], similar to the TFE driven by SP resonances [Figs. 1(b) and 1(c)].

We then consider an electron beam centered on the nanohole, where it interacts with the TFE. Regarding the electron deflection observed in Fig. 2, it is conceivable that the electrons could be deflected azimuthally by transferring a nonzero OAM to the TFE. We assume the magnetic field is localized near the hole and rapidly diminishes along the $\hat{z}$ direction, making the rotation of the electron beam induced by the magnetic field negligible [63,64]. The incident electrons are assumed to have a Gaussian wave function, given by $\psi^i(\mathbf{r}) = \psi^i_\perp(R)e^{ik_i z}$, where $\psi^i_\perp(R) = e^{-R^2/w^2}/\sqrt{\pi}w$, R is the radial coordinate, and w is the beam waist. We focus on the transition probability to final states of specific OAM $m\hbar$. These transitions involve a series of final states $\psi^f(\mathbf{r}) = i^m \psi^f_\perp(R)e^{im\phi}e^{ik_f z}/\sqrt{2\pi}$, where $\psi^f_\perp(R) = J_m(k_\perp R)/\sqrt{A_m}$, A_m is the transverse normalization area, and J_m is the mth Bessel function. Using this information as input, the total transition probability to states with OAM $m\hbar$ can be determined by Eq. (5), with [50]

$$\Gamma_{m,0}(\omega) = \sum_f \int R\, dR \int R'\, dR' \times \psi^i_\perp(R)\psi^i_\perp(R')$$
$$\times \psi^f_\perp(R)\psi^f_\perp(R')\beta(R,R',\omega),$$

where $\beta(R,R',\omega) = e^2(\pi\hbar\omega^2)^{-1}\int e^{im\phi}d\phi\int dz\,dz'\, e^{-i\omega(z-z')/v} \times \mathbb{G}_{zz}(R,\phi,z;R',\phi'=0,z';\omega)$, and the summation runs over transverse electron momentum (in the $x-y$ plane). We employ the FEM to calculate β, by introducing a classical line current input at various positions along $(\phi'=0, R')$ and then performing the integral.

The calculated transition probabilities to final states with different energies and OAM $\pm \hbar$ are presented in Fig. 3(e). Similar to the electron deflection mechanism revealed in Figs. 1(c) and 2, the preferred OAM of the transmitted electrons aligns with the TFE direction in the nanohole shown in Fig. 3(c). For instance, in the frequency ranges with anticlockwise propagating TFE [blue peaks in Fig. 3(e)], the electrons preferentially release thermal photons with the same OAM ($-\hbar$), resulting in scattered electrons with an OAM of $+\hbar$ [peaks in the solid curve, Fig. 3(e)]. The same holds for the clockwise propagating TFE. Additionally, the TFE magnitude, and thus the

scattering asymmetry to final states with OAM of $\pm\hbar$, can be enhanced by increasing the temperature or the magnetic field strength [Fig. 3(f)].

Conclusions—In this Letter, we present a feasible approach for investigating TFE by exploiting their interaction with electron beams. This method not only leads to probing the experimentally unconfirmed TFE, but also includes new manipulations to the scattered electron wave function. Measuring the dispersion of surface excitations using angle-resolved electron microscopy has been long achieved [47]. In the results shown in Fig. 2, the deflection angle is widely distributed, up to 10 μrad. Experimentally, achieving such angular resolution requires using an electron beam with an initial divergence smaller than the deflection to be measured, or more precisely in experimental terms, a large lateral coherence length. Recent studies using electron beams with low divergence have achieved angular resolutions of approximately 1 μrad [48], which is sufficient for measuring the predicted effect. Additionally, other mechanisms, such as the possible deflections caused by the magnetic field, are negligibly small compared to the effects shown in Fig. (2) [50]. While previous studies have explored electron-vortex conversion in chiral structures [56–60], our proposed technique offers higher tunability by controlling magnetic fields and temperature. Our calculations primarily consider structures at room temperature, yet higher electron temperatures, attainable through laser pulse heating, amplify the effects demonstrated herein. This study underscores the potential of electron microscopy in uncovering exotic physics associated with thermal fields in nanophotonics.

[1] K. Y. Bliokh, A. Y. Bekshaev, and F. Nori, Extraordinary momentum and spin in evanescent waves, Nat. Commun. **5**, 3300 (2014).

[2] K. Y. Bliokh, D. Smirnova, and F. Nori, Quantum spin Hall effect of light, Science **348**, 1448 (2015).

[3] Z. Yu, G. Veronis, Z. Wang, and S. Fan, One-way electromagnetic waveguide formed at the interface between a plasmonic metal under a static magnetic field and a photonic crystal, Phys. Rev. Lett. **100**, 023902 (2008).

[4] V. V. Temnov, G. Armelles, U. Woggon, D. Guzatov, A. Cebollada, A. Garcia-Martin, J.-M. Garcia-Martin, T. Thomay, A. Leitenstorfer, and R. Bratschitsch, Active magneto-plasmonics in hybrid metal–ferromagnet structures, Nat. Photonics **4**, 107 (2010).

[5] A. R. Davoyan and N. Engheta, Nonreciprocal rotating power flow within plasmonic nanostructures, Phys. Rev. Lett. **111**, 047401 (2013).

[6] A. R. Davoyan and N. Engheta, Theory of wave propagation in magnetized near-zero-epsilon metamaterials: Evidence for one-way photonic states and magnetically switched transparency and opacity, Phys. Rev. Lett. **111**, 257401 (2013).

[7] A. Davoyan and N. Engheta, Electrically controlled one-way photon flow in plasmonic nanostructures, Nat. Commun. **5**, 5250 (2014).

[8] D. Jin, L. Lu, Z. Wang, C. Fang, J. D. Joannopoulos, M. Soljačić, L. Fu, and N. X. Fang, Topological magneto-plasmon, Nat. Commun. **7**, 13486 (2016).

[9] S. Buddhiraju, Y. Shi, A. Song, C. Wojcik, M. Minkov, I. A. Williamson, A. Dutt, and S. Fan, Absence of unidirectionally propagating surface plasmon-polaritons at nonreciprocal metal-dielectric interfaces, Nat. Commun. **11**, 674 (2020).

[10] F. D. M. Haldane and S. Raghu, Possible realization of directional optical waveguides in photonic crystals with broken time-reversal symmetry, Phys. Rev. Lett. **100**, 013904 (2008).

[11] Z. Wang, Y. D. Chong, J. D. Joannopoulos, and M. Soljačić, Reflection-free one-way edge modes in a gyromagnetic photonic crystal, Phys. Rev. Lett. **100**, 013905 (2008).

[12] Z. Wang, Y. Chong, J. D. Joannopoulos, and M. Soljačić, Observation of unidirectional backscattering-immune topological electromagnetic states, Nature (London) **461**, 772 (2009).

[13] D. Jin, T. Christensen, M. Soljačić, N. X. Fang, L. Lu, and X. Zhang, Infrared topological plasmons in graphene, Phys. Rev. Lett. **118**, 245301 (2017).

[14] D. Pan, R. Yu, H. Xu, and F. J. García de Abajo, Topologically protected Dirac plasmons in a graphene superlattice, Nat. Commun. **8**, 1243 (2017).

[15] L. Zhu and S. Fan, Persistent directional current at equilibrium in nonreciprocal many-body near field electromagnetic heat transfer, Phys. Rev. Lett. **117**, 134303 (2016).

[16] M. G. Silveirinha, Topological angular momentum and radiative heat transport in closed orbits, Phys. Rev. B **95**, 115103 (2017).

[17] M. G. Silveirinha, Quantized angular momentum in topological optical systems, Nat. Commun. **10**, 349 (2019).

[18] M. G. Silveirinha, Proof of the bulk-edge correspondence through a link between topological photonics and fluctuation-electrodynamics, Phys. Rev. X **9**, 011037 (2019).

[19] D. Gelbwaser-Klimovsky, N. Graham, M. Kardar, and M. Krüger, Near field propulsion forces from nonreciprocal media, Phys. Rev. Lett. **126**, 170401 (2021).

[20] D. Pan, H. Xu, and F. J. García de Abajo, Magnetically activated rotational vacuum friction, Phys. Rev. A **99**, 062509 (2019).

[21] Y. Guo and S. Fan, Single gyrotropic particle as a heat engine, ACS Photonics **8**, 1623 (2021).

[22] M. F. Maghrebi, A. V. Gorshkov, and J. D. Sau, Fluctuation-induced torque on a topological insulator out of thermal equilibrium, Phys. Rev. Lett. **123**, 055901 (2019).

[23] G. Tang, L. Zhang, Y. Zhang, J. Chen, and C. T. Chan, Near-field energy transfer between graphene and magneto-optic media, Phys. Rev. Lett. **127**, 247401 (2021).

[24] B. Barwick, D. J. Flannigan, and A. H. Zewail, Photon-induced near-field electron microscopy, Nature (London) **462**, 902 (2009).

[25] F. J. García de Abajo, A. Asenjo Garcia, and M. Kociak, Multiphoton absorption and emission by interaction of swift electrons with evanescent light fields, Nano Lett. **10**, 1859 (2010).

[26] S. T. Park, M. Lin, and A. H. Zewail, Photon-induced near-field electron microscopy (PINEM): Theoretical and experimental, New J. Phys. **12**, 123028 (2010).

[27] S. T. Park and A. H. Zewail, Relativistic effects in photon-induced near field electron microscopy, J. Phys. Chem. A **116**, 11128 (2012).

[28] F. O. Kirchner, A. Gliserin, F. Krausz, and P. Baum, Laser streaking of free electrons at 25 keV, Nat. Photonics **8**, 52 (2014).

[29] L. Piazza, T. T. A. Lummen, E. Quiñonez, Y. Murooka, B. Reed, B. Barwick, and F. Carbone, Simultaneous observation of the quantization and the interference pattern of a plasmonic near-field, Nat. Commun. **6**, 6407 (2015).

[30] A. Feist, K. E. Echternkamp, J. Schauss, S. V. Yalunin, S. Schäfer, and C. Ropers, Quantum coherent optical phase modulation in an ultrafast transmission electron microscope, Nature (London) **521**, 200 (2015).

[31] T. T. A. Lummen, R. J. Lamb, G. Berruto, T. LaGrange, L. D. Negro, F. J. García de Abajo, D. McGrouther, B. Barwick, and F. Carbone, Imaging and controlling plasmonic interference fields at buried interfaces, Nat. Commun. **7**, 13156 (2016).

[32] K. E. Echternkamp, A. Feist, S. Schäfer, and C. Ropers, Ramsey-type phase control of free-electron beams, Nat. Phys. **12**, 1000 (2016).

[33] G. M. Vanacore, A. W. P. Fitzpatrick, and A. H. Zewail, Four-dimensional electron microscopy: Ultrafast imaging, diffraction and spectroscopy in materials science and biology, Nano Today **11**, 228 (2016).

[34] M. Kozák, J. McNeur, K. J. Leedle, H. Deng, N. Schönenberger, A. Ruehl, I. Hartl, J. S. Harris, R. L. Byer, and P. Hommelhoff, Optical gating and streaking of free electrons with sub-optical cycle precision, Nat. Commun. **8**, 14342 (2017).

[35] A. Feist, N. Bach, T. D. N. Rubiano da Silva, M. Mäller, K. E. Priebe, T. Domröse, J. G. Gatzmann, S. Rost, J. Schauss, S. Strauch, R. Bormann, M. Sivis, S. Schäfer, and C. Ropers, Ultrafast transmission electron microscopy using a laser-driven field emitter: Femtosecond resolution with a high coherence electron beam, Ultramicroscopy **176**, 63 (2017).

[36] K. E. Priebe, C. Rathje, S. V. Yalunin, T. Hohage, A. Feist, S. Schäfer, and C. Ropers, Attosecond electron pulse trains and quantum state reconstruction in ultrafast transmission electron microscopy, Nat. Photonics **11**, 793 (2017).

[37] A. Ryabov and P. Baum, Electron microscopy of electromagnetic waveforms, Science **353**, 374 (2016).

[38] Y. Morimoto and P. Baum, Attosecond control of electron beams at dielectric and absorbing membranes, Phys. Rev. A **97**, 033815 (2018).

[39] G. M. Vanacore, I. Madan, G. Berruto, K. Wang, E. Pomarico, R. J. Lamb, D. McGrouther, I. Kaminer, B. Barwick, F. J. García de Abajo, and F. Carbone, Attosecond coherent control of free-electron wave functions using semi-infinite light fields, Nat. Commun. **9**, 2694 (2018).

[40] R. Dahan, S. Nehemia, M. Shentcis, O. Reinhardt, Y. Adiv, X. Shi, O. Be'er, M. H. Lynch, Y. Kurman, K. Wang *et al.*, Resonant phase-matching between a light wave and a free-electron wavefunction, Nat. Phys. **16**, 1123 (2020).

[41] O. Kfir, H. Lourenço-Martins, G. Storeck, M. Sivis, T. R. Harvey, T. J. Kippenberg, A. Feist, and C. Ropers, Controlling free electrons with optical whispering-gallery modes, Nature (London) **582**, 46 (2020).

[42] K. Wang, R. Dahan, M. Shentcis, Y. Kauffmann, A. Ben Hayun, O. Reinhardt, S. Tsesses, and I. Kaminer, Coherent interaction between free electrons and a photonic cavity, Nature (London) **582**, 50 (2020).

[43] R. Shiloh, T. Chlouba, and P. Hommelhoff, Quantum-coherent light-electron interaction in a scanning electron microscope, Phys. Rev. Lett. **128**, 235301 (2022).

[44] R. Dahan, A. Gorlach, U. Haeusler, A. Karnieli, O. Eyal, P. Yousefi, M. Segev, A. Arie, G. Eisenstein, P. Hommelhoff *et al.*, Imprinting the quantum statistics of photons on free electrons, Science **373**, eabj7128 (2021).

[45] N. Rivera, L. J. Wong, J. D. Joannopoulos, M. Soljačić, and I. Kaminer, Light emission based on nanophotonic vacuum forces, Nat. Phys. **15**, 1284 (2019).

[46] V. Di Giulio and F. J. García de Abajo, Electron diffraction by vacuum fluctuations, New J. Phys. **22**, 103057 (2020).

[47] R. B. Pettit, J. Silcox, and R. Vincent, Measurement of surface-plasmon dispersion in oxidized aluminum films, Phys. Rev. B **11**, 3116 (1975).

[48] A. Feist, S. V. Yalunin, S. Schäfer, and C. Ropers, High-purity free-electron momentum states prepared by three-dimensional optical phase modulation, Phys. Rev. Res. **2**, 043227 (2020).

[49] O. Madelung, *Semiconductors: Data Handbook* (Springer-Verlag, Berlin, Heidelberg, 2004).

[50] See Supplemental Material at http://link.aps.org/supplemental/10.1103/PhysRevLett.133.113805 for detailed derivations of the fluctuation-dissipation theorem, a general framework for describing TFE and its interaction with electron beams, applications of this theory to planar surfaces and nanodisk structures, an estimation of the non-local correction to the nanodisk, and a discussion on the possible electron deflection caused by the magnetic field.

[51] B. Huttner and S. M. Barnett, Quantization of the electromagnetic field in dielectrics, Phys. Rev. A **46**, 4306 (1992).

[52] H. T. Dung, L. Knöll, and D.-G. Welsch, Three-dimensional quantization of the electromagnetic field in dispersive and absorbing inhomogeneous dielectrics, Phys. Rev. A **57**, 3931 (1998).

[53] S. Y. Buhmann, D. T. Butcher, and S. Scheel, Macroscopic quantum electrodynamics in nonlocal and nonreciprocal media, New J. Phys. **14**, 083034 (2012).

[54] L. Novotny and B. Hecht, *Principles of Nano-Optics* (Cambridge University Press, New York, 2006).

[55] F. J. García de Abajo, Optical excitations in electron microscopy, Rev. Mod. Phys. **82**, 209 (2010).

[56] K. Y. Bliokh, Y. P. Bliokh, S. Savel'ev, and F. Nori, Semi-classical dynamics of electron wave packet states with phase vortices, Phys. Rev. Lett. **99**, 190404 (2007).

[57] J. Verbeeck, H. Tian, and P. Schattschneider, Production and application of electron vortex beams, Nature (London) **467**, 301 (2010).

[58] S. M. Lloyd, M. Babiker, G. Thirunavukkarasu, and J. Yuan, Electron vortices: Beams with orbital angular momentum, Rev. Mod. Phys. **89**, 035004 (2017).

[59] K. Y. Bliokh, I. P. Ivanov, G. Guzzinati, L. Clark, R. Van Boxem, A. Béché, R. Juchtmans, M. A. Alonso, P. Schattschneider, F. Nori, and J. Verbeeck, Theory and applications of free-electron vortex states, Phys. Rep. **690**, 1 (2017).

[60] A. Asenjo-Garcia and F. J. García de Abajo, Dichroism in the interaction between vortex electron beams, plasmons, and molecules, Phys. Rev. Lett. **113**, 066102 (2014).

[61] N. A. Mortensen, S. Raza, M. Wubs, T. Søndergaard, and S. I. Bozhevolnyi, A generalized non-local optical response theory for plasmonic nanostructures, Nat. Commun. **5**, 3809 (2014).

[62] T. Christensen, W. Yan, A.-P. Jauho, M. Soljačić, and N. A. Mortensen, Quantum corrections in nanoplasmonics: Shape, scale, and material, Phys. Rev. Lett. **118**, 157402 (2017).

[63] K. Y. Bliokh, P. Schattschneider, J. Verbeeck, and F. Nori, Electron vortex beams in a magnetic field: A new twist on Landau levels and Aharonov-Bohm states, Phys. Rev. X **2**, 041011 (2012).

[64] G. Guzzinati, P. Schattschneider, K. Y. Bliokh, F. Nori, and J. Verbeeck, Observation of the Larmor and Gouy rotations with electron vortex beams, Phys. Rev. Lett. **110**, 093601 (2013).